J. Marine Sci. Appl. (2012) 11: 295-300
DOI: 10.1007/s11804-012-1135-0

Analysis of a Propeller Wake Flow Field Using Viscous Fluid Mechanics

Miao He*, Chao Wang, Xin Chang and Sheng Huang

College of Shipbuilding Engineering, Harbin Engineering University, Harbin 150001, China

Abstract: The computational fluid dynamics (CFD) method is used to numerically simulate a propeller wake flow field in open water. A sub-domain hybrid mesh method was adopted in this paper. The computation domain was separated into two sub-domains, in which tetrahedral elements were used in the inner domain to match the complicated geometry of the propeller, while hexahedral elements were used in the outer domain. The mesh was locally refined on the propeller surface and near the wake flow field, and a size function was used to control the growth rate of the grid. Sections at different axial location were used to study the spatial evolution of the propeller wake in the region ranging from the disc to one propeller diameter (*D*) downstream. The numerical results show that the axial velocity fluctuates along the wake flow; radial velocity, which is closely related to vortices, attenuates strongly. The trailing vortices interact with the tip vortex at the blades' trailing edge and then separate. The strength of the vortex shrinks rapidly, and the radius decreases 20% at one diameter downstream.

Keywords: computational fluid dynamics (CFD); viscous fluid mechanics; sub-domain hybrid mesh; wake velocity field
Article ID: 1671-9433(2012)03-0295-06

1 Introduction

Accurate prediction of propeller wake flow has an important effect on evaluating propeller hydrodynamic performance, supervising propeller optimization, and designing an energy saving rudder. The research on wake behind a propeller mainly focuses on experimental analysis (Jessup, 1998; Paik *et al*., 2007; Stella *et al*., 2000). However, due to the length and high cost of experimentation, the research has only been carried out in theory. According to the papers published, the calculations were done by potential flow theory (Su *et al.*, 2002; Ye *et al.*, 2008) in which the wake shape was assumed and the spatial evolution of the propeller wake could not be accurately simulated. For the rapid development of the viscosity fluid dynamic method, more and more researchers have been focusing on predicting propeller hydrodynamics by CFD (Krasilnikov *et al*., 2009; Mitja and Enrico, 2009; Watanabe *et al*., 2003), but they seem to be more interested in hydrodynamic performance of propellers, pressure distribution on the blade surface, generation of the tip vortex, and working less with the detailed spatial evolution process of a propeller wake.

In the present study, a numerical simulation model was set up to investigate the spatial evolution process of the propeller wake in detail between the area ranging from the disc to one propeller diameter (*D*) downstream. The changing rules of velocity and vortex were obtained by analyzing contours at different sections along the axis direction.

2 Numerical model

2.1 Governing equations

Hydrokinetic governing equations contain a series of differential equations such as continuity equations, Navier-Stokes equations, and energy conservation equations. For liquids such as water in which the propeller rotation is incompressible and the density is constant considering that there is no heat exchange, the continuity equations can be written as

$$\frac{\partial u_i}{\partial x_i} = 0 \tag{1}$$

Navier-Stokes equations can be written as

$$\frac{\partial(\rho u_i)}{\partial t} + \frac{\partial(\rho u_i u_j)}{\partial x_j} = -\frac{\partial p}{\partial x_i} + \frac{\partial}{\partial x_j}(\mu \frac{\partial u_i}{\partial x_j} - \rho \overline{u_i' u_j'}) \tag{2}$$

where u_i, u_j are time-average velocity $(i, j = 1, 2, 3)$, p is the time-average pressure, ρ the density, μ the viscosity coefficient, and $-\rho \overline{u_i' u_j'}$ the Reynolds stress item which is unknown. The equations are not closed and a new turbulence equation is added into the system.

2.2 Turbulence model

The turbulence model used in this research is a re-normalization group (RNG) $k-\varepsilon$ model because the RNG model is more likely to be susceptible to instability in steady-state solutions, in which two additional transport

Received date: 2011-05-27.
Foundation item: Supported by Fundamental Research Funds for the Central Universities (Grant No. HEUCFT1001) and Ph.D Programs Foundation of Ministry of Education of China (Grant No. 10702016).
***Corresponding author Email:** miaomiao591213@yahoo.com.cn

equations (for the turbulence kinetic energy k and the turbulence dissipation rate ε) are solved. The equation can be written as

$$\frac{\partial(\rho k)}{\partial t}+\frac{\partial}{\partial x_i}(\rho U_i k)=\frac{\partial}{\partial x_j}\left[\alpha_k \mu_{\text{eff}}\frac{\partial k}{\partial x_j}\right]+G_k+\rho\varepsilon \quad (3)$$

$$\frac{\partial \rho\varepsilon}{\partial t}+\frac{\partial}{\partial x_i}(\rho u_i \varepsilon)=\frac{\partial}{\partial x_j}\left[\alpha_\varepsilon u_{\text{eff}}\frac{\partial \varepsilon}{\partial x_j}\right]+\frac{C_{1\varepsilon}^*}{k}G_k-C_{2\varepsilon}\rho\frac{\varepsilon^2}{k} \quad (4)$$

where $\mu_{\text{eff}}=\mu+\mu_t$, $\mu_t=\rho C_\mu\frac{k^2}{\varepsilon}$, $C_\mu=0.0845$, $\alpha_K=\alpha_\varepsilon=1.39$,

$C_{1\varepsilon}^*=C_{1\varepsilon}-\frac{\eta(1-\eta/\eta_0)}{1+\beta\eta^3}$, $C_{1\varepsilon}=1.42$, $C_{2\varepsilon}=1.68$, $\eta=(2E_{ij}.E_{ij})^{1/2}\frac{k}{\varepsilon}$,

$E_{ij}=\frac{1}{2}(\frac{\partial u_i}{\partial x_j}+\frac{\partial u_j}{\partial x_i})$, $\eta_0=4.377$, $\beta=0.012$.

2.3 Numerical method

The incompressible three-dimensional RANS equations are used to simulate three-dimensional flow fields. The finite volume method is used to discrete governing equations in the computational domain, and the central-difference scheme is adopted in the diffusion term while the first-order upwind scheme is used in the convection term. The coupling arithmetic of velocity and pressure is known as the semi-Implicit method for pressure-linked equations (SIMPLE). The result is convergence when the continuity curve is less than 0.000 1.

3 Geometry and computation grid

The computation performed for Propeller DTRC4119 detailed the data of the flow field and showed a standard propeller to validate the precision of numerical simulation by the International Towing Tank Conference (ITTC). A detailed description of the geometry is shown in Table 1.

Table 1 Geometry coefficients of the propeller

Geometry parameter	DTRC4119
Diameter /m	0.3048
Number of blades	3
Hub ratio	0.2
Area ratio	0.6
Pitch ratio/ 0.7R	1.084
Rake angle/(°)	0
Skew angle/(°)	0
Section	NACA66(mod)

Two kinds of coordinate systems were used here: the Cartesian system $o-xyz$ and cylindrical system $o-xr\theta$. The origin o is fixed at the central point of the propeller. In the Cartesian coordinate system, the x axis is down the slipstream along the propeller shaft, the y axis is the generatrix of a blade, and the z axis follows a right-hand rule with the x and y axis. In the $o-xr\theta$ system, θ is measured counter-clockwise from the y axis, as shown in Fig. 1.

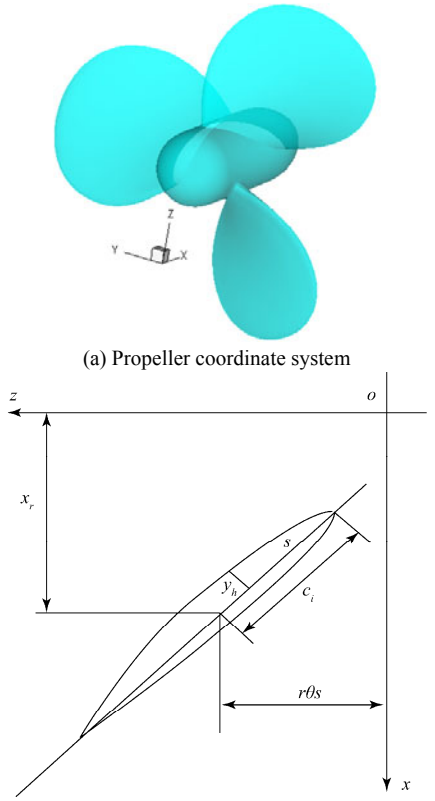

(a) Propeller coordinate system

(b) Blade section

Fig. 1 Geometry model of the propeller

According to the theory above, a program was used to transform coordinates of local points on sections to the global coordinates in FORTRAN, and the computation model was built in a commercial grid generator known as the integrated computer engineering and manufacturing code for computational fluid dynamics (ICEMCFD). The cylindrical computation domain, whose diameter is 5 times the propeller diameter and length is 12 times the propeller diameter, is divided into two parts, with the propeller in the inner part. The single rotating reference frame fixed on the propeller rotates with an angular velocity of −600 r/min, and the outer domain is steady. The information of the two domains is interpolated and transferred by the interface boundary. A constant velocity boundary condition is specified at the inlet. The pressure outlet boundary is prescribed at the outflow, and a periphery cylinder is set as a non-slip wall boundary.

The grid quality directly influences the convergence and precision of numerical results. Considering the twist geometry of the propeller, a hybrid mesh approach is used here. An unstructured grid is used in the inner computation domain, and a structured grid is used in the outer domain. The grid is locally refined on the blade surface and its neighborhood, and the size function is imposed to control grid density transition. In the present work, 3.2 million elements were used, among which approximately 2.3 million were nearby the propeller. The grid detail is shown in Fig. 2.

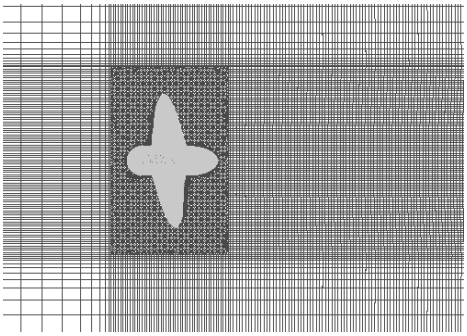

(a) Mesh in outer domain

(b) Mesh in inner domain

Fig. 2 Mesh in calculation domain

4 Numerical results

4.1 Validation of propeller performance in open water

The non-dimensional parameters are described as follows:

$$J=\frac{V_0}{nD},\quad K_T=\frac{T}{\rho n^2 D^4},\quad K_Q=\frac{Q}{\rho n^2 D^5}$$

where ρ is the fluid density, n the propeller rotational speed, D the diameter of propeller, V_0 the inflow velocity, K_T the thrust coefficient, and K_Q the torque coefficient of the propeller.

Table 2 Open water performance of the propeller

J	K_T (Exp.)	K_Q (Exp.)	K_T (Cal.)	K_Q (Cal.)	K_T (Error%)	K_Q (Error%)
0.5	0.285	0.477	0.280	0.480	−1.754	0.629
0.7	0.200	0.360	0.197	0.370	−1.500	2.778
0.806	0.157	0.296	0.156	0.295	−0.637	−0.338
0.833	0.146	0.280	0.145	0.285	−0.685	1.786
0.9	0.120	0.239	0.118	0.242	−1.667	1.255
1.1	0.034	0.106	0.033	0.103	−2.353	−2.830

In Table 2, the comparison of computational results with experimental data is shown (Su and Huang, 2003). Note that the hydrodynamic performance of calculation meshes well with the experimental results. The max error of K_T is 2.353%, and the max error of K_Q is 2.83%, which means this method is reliable in predicting the hydrodynamic performance of a propeller.

4.2 Validation of velocity in flow filed

The velocity distribution at $x/R=0.295$, $r/R=0.7$ is shown in Fig. 4. After comparison with the experimental data, it can be seen that the calculation data coincides well with the experimental data except in the peak position. The reason is that the peak area is narrow and the grid density can't meet the demand due to the limitations of the computer; on the other hand, the turbulence model influences the numerical results because the turbulence dissipation rate ε is an empirical equation and Reynolds stresses are linear which are different from the actual example.

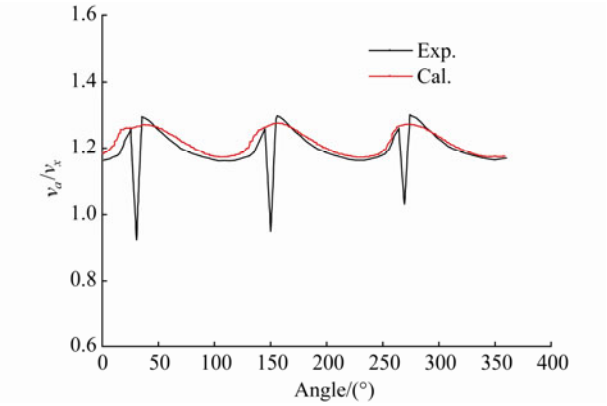

(a) Axial velocity

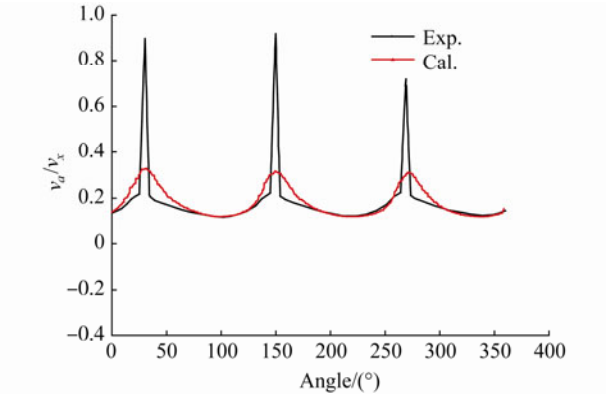

(b) Tangential velocity

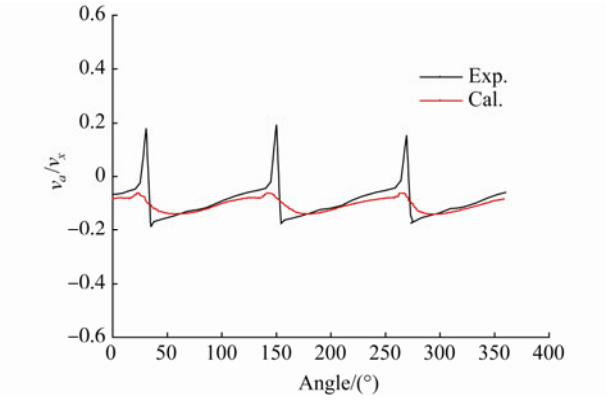

(c) Radial velocity

Fig. 3 Calculated velocity results of wake

4.3 Analysis of velocity field in near-propeller wake flow

The changing rules of velocity and vortex along the shaft axis

are analyzed here. In actual cases, induced velocity can be measured far behind the propeller because of its strong disturbance, so it is not easy to study the whole wake flow. In this paper, the wake flow behind the propeller is separated into two parts – the near-propeller wake region and far-propeller wake region – and the near-propeller region ranges from the disc to one diameter of the propeller downstream. The spatial evolution of the propeller wake is described at eight transversal sections along the propeller axis $x/R = 0.0,\ 0.196\,9,\ 0.382\,1,\ 0.656\,2,\ 1.0,\ 1.312\,4,\ 1.6,\ 2.0$ under the advance ratio $J = 0.833$.

4.3.1 Numerical results of axial velocity

The propeller obtains thrust by the reaction force of axial velocity. Axial velocity contours at different sections are shown in Fig. 4.

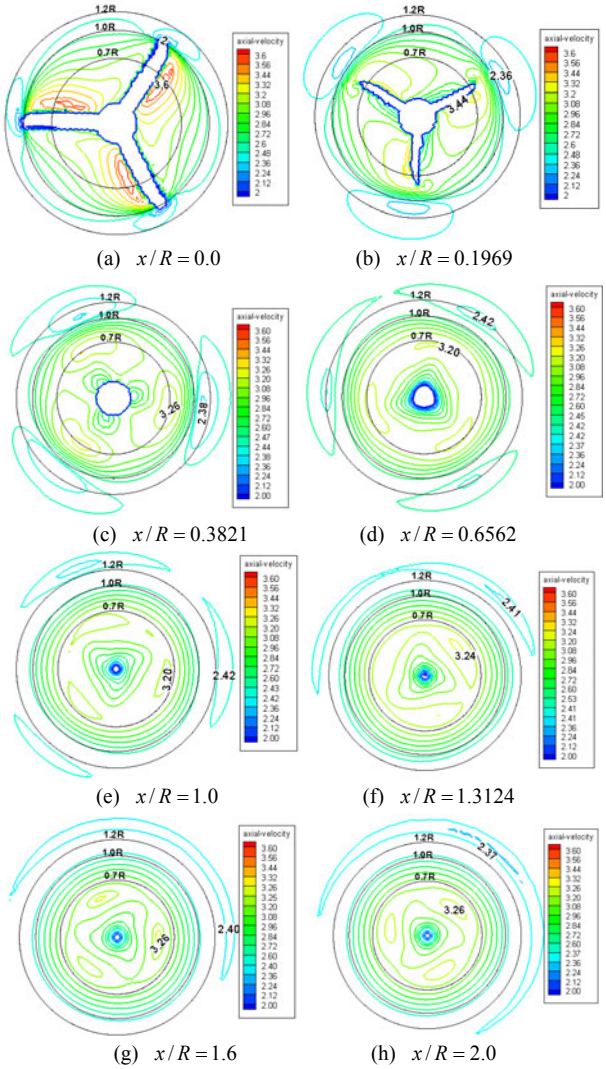

(a) $x/R = 0.0$ (b) $x/R = 0.1969$

(c) $x/R = 0.3821$ (d) $x/R = 0.6562$

(e) $x/R = 1.0$ (f) $x/R = 1.3124$

(g) $x/R = 1.6$ (h) $x/R = 2.0$

Fig. 4 Axial velocity contours of wake flow

In Fig. 4(a), the axial velocity contour is shown to be x/R=0.0; closed low-speed regions formed near the blade tip, and closed high-speed regions formed on the suction face near $0.7R$. The contour-lines at the blade tip extended to the opposite direction of rotation. The radial gradients of iso-velocity along the circle were asymmetrical, and the gradients were at the maximum at the pressure face while at the minimum between the two blades. While $0.0 \le x/R \le 0.656\,2$, as shown in Figs. 4(a)–(d), because the effect of energy transfer is greater than viscosity dissipation between the high-speed region at $0.7R$ and the low-speed region at the blade tip, the area of the low-speed region increases while the central position is moving out in a radial direction and speed is accelerating; the velocity of the high-speed region slows down. When $x/R = 1.0$, as shown in Figs. 4(e), while the energy exchange and viscosity dissipation keep balance, the velocity of the two regions stays basically constant. While $x/R > 1.0$, as shown in Figs. 4(f)–(h), the distribution of contour-lines between the two regions is a series of concentric circles. The viscosity dissipation plays a leading role in the low-speed region, so the velocity decelerates gradually, and borderlines in the low-speed region disappear. The velocity in the high-speed region at $0.7R$ increases slightly for energy transfer from a nearby high-speed region behind the hub. At $x/R = 2.0$, the distribution of contour-lines between the high-speed region at $0.7R$ and the low-speed region at the blade tip is a series of concentric circles.

4.3.2 Numerical results of radial velocity

Radial velocity is an important composition of wake vortex, and the value is considered positive along the radial direction. Fig. 5 shows the contours of radial velocity at different axial positions.

The wake flow between the disc and trailing edge is shown in Figs. 5(a)–(b). It can be seen that periodic positive and negative velocity regions exist at the blade tip and heel. This means that by the effect of axial velocity, there are pairs of vortices with different directions yielded at the blade tip and heel. Along the wake flow downstream, as shown in Figs. 5(c)–(h), positive regions at the blade tip merge with the heel region of the same blade while the negative blade tip region merges with the heel region of the next blade. Both the absolute velocity values of the positive and negative areas decay and the centers of the closed contour-lines move inward along the radial direction. At x/R=2.0, there are six closed velocity regions in the flow field and the absolute value is almost 0.

4.3.3 Numerical results of tangential velocity

Fig. 6 shows the tangential velocity contours at different axial positions. In the propeller disk, the velocity is negative, while a positive velocity region exists at the blade tip out of the disk, which is the effect of tangential velocity on the tip vortex. The positive region at the blade tip decays rapidly and disappears at x/R<0.3821, as shown in Figs. 6(a)–(b). The distribution of tangential velocity gradients behind the propeller is gradually uniform along the radial direction and the contour-lines

become a series of concentric circles in the end.

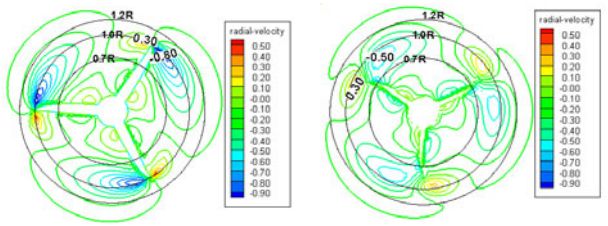

(a) $x/R=0.0$ (b) $x/R=0.1969$

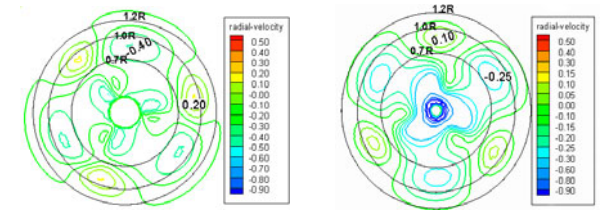

(c) $x/R=0.3821$ (d) $x/R=0.6562$

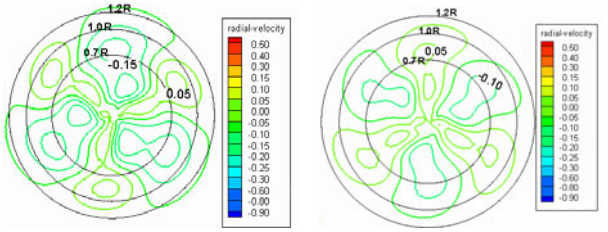

(e) $x/R=1.0$ (f) $x/R=1.3124$

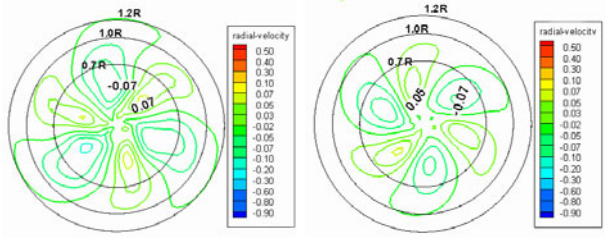

(g) $x/R=1.6$ (h) $x/R=2.0$

Fig. 5 Radial velocity contours of wake flow

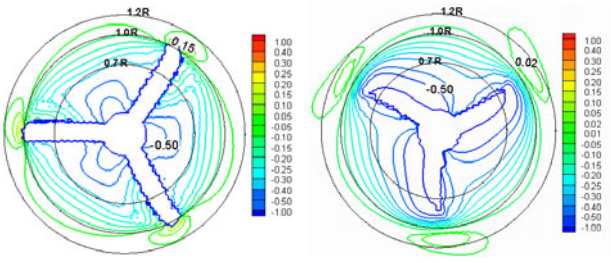

(a) $x/R=0.0$ (b) $x/R=0.1969$

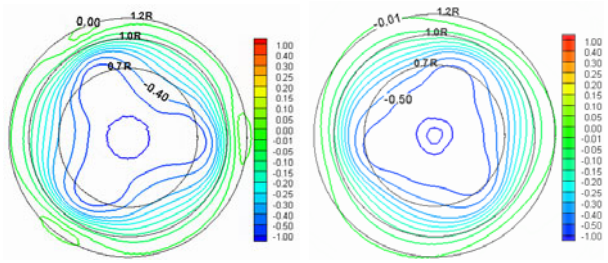

(c) $x/R=0.3821$ (d) $x/R=0.6562$

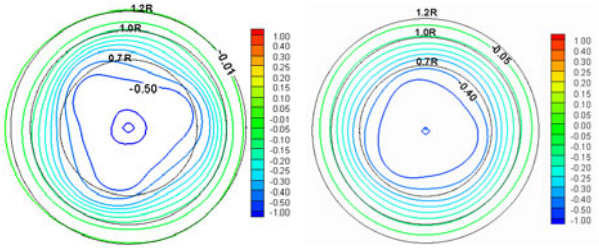

(e) $x/R=1.0$ (f) $x/R=2.0$

Fig. 6 Tangential velocity contours of wake flow

In general, the impact area of tangential velocity is smaller than that of radial velocity, and the evolution rule is simpler. The velocity in the propeller disk is negative and the positive region at the blade tip declines rapidly. The contour-lines are uniformly distributed concentric circles.

4.3.4 Numerical results of wake vortex

Fig. 7 shows the spatial evolution of the vortex structure in the wake region. Trailing vortices can be observed behind the following edge of the blade as well as tip and hub vortices in the slipstream region. The trailing vortices were caused by the viscosity boundary layer of the blade. As the wake moved downstream, the wake sheet began to have a larger slope with respect to the x/D axis. The strength and radius of the vortex decays rapidly further downstream. The radius of the tip vortex declines by about 20% at $x/D=1.0$.

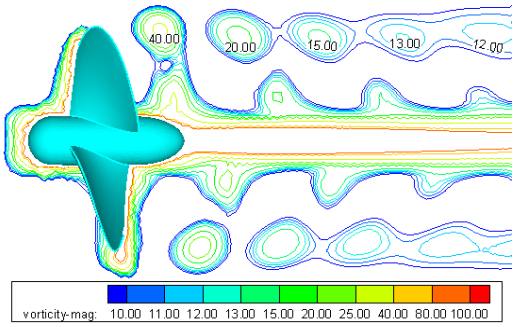

Fig. 7 Vortex contour of wake field (longitudinal profile)

5 Conclusions

The evolution characteristics of the propeller wake in the region ranging from the disc to one propeller diameter (D) downstream were investigated by using the CFD method. Some conclusions can be drawn as follows:

The method is accurate in predicting the hydrodynamic performance of a propeller and velocity distribution in the region near the propeller.

For axial velocity, low-speed regions exist at the blade tip and high-speed regions exist on the pressure surface at $0.7R$ and behind the hub in the free slipstream. Due to imbalance of energy exchange and viscosity dissipation between high-speed and low-speed areas, the velocity at the blade tip

first accelerates and then decelerates, and the rule of changes in velocity at $0.7R$ is the opposite.

The radial velocity wake flow contours are complex. Vortex by radial velocity exists at the blade tip and heel. Along the axis, velocity regions merge and decay rapidly. Pairs of negative and positive velocity regions appear on the blade tip and heel alternatively along the circumferential direction. At x/R=2.0, absolute velocity is close to 0.

Vortices such as the tip, trailing, and hub vortices can be observed at a longitudinal profile, and the trailing vortices interact with the tip vortex near behind blades. The strength shrinks rapidly downstream, and the radius decreases by about 20% at x/R=2.0.

References

Jessup SD (1998). An experimental investigation of viscous aspects of propeller. *The 22nd ITTC Propulsion Committee Propeller RANS/Panel Method Workshop Proceedings*, Washington, 200-205.

Krasilnikov V, Sun Jiaying, Halse KH (2009). CFD investigation in scale effect on propellers with different magnitude of skew in turbulent flow. *The First International Symposium on Marine Propulsors*, Trondheim, 25-40.

Mitja M, Enrico N (2009). Comparison of hexa-structured and hybrid-unstructured meshing approaches for numerical prediction of the flow around marine propellers. *The First International Symposium on Marine Propulsors*, Trondheim, 500-507.

Paik BG, Kim J, Park YH, Kim KS, Yu KK (2007). Analysis of wake behind a rotating propeller using PIV technique in a cavitation tunnel. *Ocean Engineering*, **34**, 594-604.

Stella A, Guy G, Di Felice F (2000). Propeller wake flow field analysis by means of LDV phase sampling technique. *Experiments in Fluids*, **28**, 1-10.

Su Yumin, Huang Sheng (2003). *Ship propeller theory*. Harbin Engineering University Press, Harbin, China, 159-160, 169.

Su Yumin, Ikehata M, Kai H (2002). Numerical analysis of the flow field around marine propellers by surface panel method. *Ocean Engineering*, **20**(3), 44-48.

Watanabe T, Kawamura T, Takekoshi Y, Maeda M, Rhee SH (2003). Simulation of steady and un-steady cavitation on a marine propeller using a rans cfdcode. *The Fifth International Symposium on Cavitation* , Osaka, 502-506.

Ye Jinming, Xiong Ying (2008). Prediction of podded propeller cavitation using an unsteady surface panel method. *Journal of hydrodynamics*, **20**(6), 790-792.

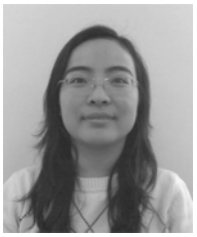

Miao He was born in 1985. She is a PhD candidate at Harbin Engineering University. Her current research interest includes ship propulsion.

Chao Wang was born in 1982. He is a doctor of Design and Construction of Naval Architecture and Ocean Structure at Harbin Engineering University. His current research interest includes marine special propulsors.

Sheng Huang was born in 1945. He is a professor of Harbin Engineering University. His current research interests include design and construction of naval architecture and ocean structure, ship propulsion, *etc*.